remote sensing

MDPI

Article

Flood Hazard Assessment Using Weather Radar Data in Athens, Greece

Apollon Bournas and Evangelos Baltas *

Department of Water Resources and Environmental Engineering, School of Civil Engineering, National Technical University of Athens, 5 Iroon Polytechniou, 157 80 Athens, Greece; abournas@chi.civil.ntua.gr
* Correspondence: baltas@chi.civil.ntua.gr

Abstract: Weather radar plays a critical role in flash flood forecasting, providing an effective and comprehensive guide for the identification of possible flood-prone areas. However, the utilization of radar precipitation data remains limited in current research and applications, particularly in addressing flash flood hazards in complex environments such as in Athens, Greece. To address this gap, this study introduces the Gridded Flash Flood Guidance (GFFG) method, a short-term flash flood forecasting and warning technology based on radar precipitation and hydrological model coupling, and implements it in the region of Athens, Greece. The GFFG system improves upon the traditional flash flood guidance (FFG) concept by better integrating the weather radar dataset's spatial and temporal flexibility, leading to increased resolution results. Results from six flood events underscore its ability to identify high-risk areas dynamically, with urban regions frequently flagged for flooding unless initial soil moisture conditions are low. Moreover, the sensitivity analysis of the system showed that the most crucial parameter apart from rainfall input is the soil moisture conditions, which define the amount of effective rainfall. This study highlights the significance of incorporating radar precipitation and real-time soil moisture assessments to improve flood prediction accuracy and provide valuable flood risk assessments.

Keywords: flood hazard; gridded flash flood guidance; soil moisture conditions; weather radar; FFG; Athens; Greece

check for updates

Academic Editors: Quoc Bao Pham, Sk Ajim Ali, Bahram Choubin, Farhana Parvin and Meriame Mohajane

Received: 11 November 2024
Revised: 21 December 2024
Accepted: 26 December 2024
Published: 28 December 2024

Citation: Bournas, A.; Baltas, E. Flood Hazard Assessment Using Weather Radar Data in Athens, Greece. *Remote Sens.* **2025**, *17*, 72. https://doi.org/10.3390/rs17010072

Copyright: © 2024 by the authors. Licensee MDPI, Basel, Switzerland. This article is an open access article distributed under the terms and conditions of the Creative Commons Attribution (CC BY) license (https://creativecommons.org/licenses/by/4.0/).

1. Introduction

Floods are one of the most devastating natural hazards, with severe consequences for human life, infrastructure, and ecosystems [1]. Although floods are usually perceived as riverside, the most catastrophic flood events are flash floods, which are sudden and rapidly developing floods characterized by their swift onset and high intensity. In most cases where fatal flash floods have been recorded, the main issue was that no proper alert was issued. As in the most recent flood event in Valencia, November 2024, with ongoing reports of over 200 human fatalities, while there was information about incoming high rainfall, no proper warning was given in the needed time frame. The same situation was recorded with the well-documented November 2017 Mandra event in Greece, which resulted in the loss of 24 human lives [2–4]. After analysis of the event [2], it was found that extreme rainfall was observed, i.e., 200 mm in six hours, at such a local scale that typical rain gauge systems could not record it, with the only measurements being made by weather radar. To that end, with floods and flash floods becoming more frequent, especially in the Mediterranean [2,3,5–8] due to the effects of climate change on the sea temperature, accurate and timely weather forecasts for mitigating flood hazards are deemed critical.

Flood hazard refers to the probability of an occurrence of a flood event and its characteristics, such as the magnitude, frequency, and duration of flooding. To examine these characteristics on the desired scale, the resolution of the datasets should be obtained to the appropriate scale. Flash floods affect urban areas and require high-resolution temporal and spatial data [9]. Apart from rainfall, other factors such as the basin's geomorphological and geological characteristics, mainly its size, slope, soil infiltration capacity, and initial soil moisture levels, also control flood generation [10–13]. Therefore, the suggested methodology for assessing flood hazards should always incorporate rainfall input and the above. To that end, recent research assessing historical events relies solely on fusing fine geomorphological datasets with weather radar datasets [14–17]. Moreover, it has also been found that utilizing weather radar in flash flood real-time assessment tends to decrease the mortality of floods, reducing the overall cost of flooding [18].

On the other hand, new research has focused on satellite datasets [3,7] to provide early warnings and flood assessments, but the main issue lies in the quality of the datasets, which denies their use for flash flood assessment [19], while it is evident that the results would be enhanced should weather radar datasets be incorporated. The most significant disadvantage of the weather radar datasets, apart from the required calibration of the radar system itself, is the availability of the datasets. Weather radar can cost a significant amount of money, and its use requires specialized personnel, whereas satellite data can be easily obtained.

Weather radar datasets work well with most real-time flood hazard assessments when available. Advances in other fields, such as improved and detailed hydrodynamic modeling, have increased the interest in using gridded rainfall datasets as in modeling [16]. However, assessing flash floods is challenging since it does not allow the required time to fully simulate the rainfall–runoff process, whereas the resolution of the results should be as fine as possible. To that end, hydrometeorological methods and systems are preferred for assessing flash flood-prone areas. In Europe, the operational system for assessing and providing flood warnings is the European Flood Awareness System (EFAS) [20]. The systems rely on the ERIC (Evaluation and Reporting Interface for Copernicus) system [21,22] and the EPICA (European Precipitation Index Climatology) system [23,24] to provide timely warnings. Of the two, only the EPICA features the required resolution to detect flash floods, featuring a 1 km $\times$ 1 km grid and up to 6 h of lead time. In order to perform this detection, the system relies on the OPERA radar composite, signifying a pivotal role in improving the resolution and accuracy of precipitation estimates [25,26]. However, the OPERA does not operate in Greece, making the country vulnerable to flash flood threats.

Another well-cited flash flood warning system is the flash flood guidance (FFG) system developed in the 1980s and still used operationally by the USA as their flash flood early warning system [27,28]. Although still operational, various implementations of the system have been reported, mainly concerning the spatial resolution approach of the generated results, such as the lumped FFG (LFFG) [29], the Flash Potential Index (FFPI) [30], the Gridded Flash Flood Guidance [31], and the Distributed Flash Flood Guidance (DFFG) [32]. Among the above, the GFFG system has shown increased potential due to the rise of satellite-derived datasets and Geographical Information Systems (GIS) tools [13]. As in the original FFG implementation, the system evaluates the FFG value, i.e., the rainfall accumulation threshold above which minor flooding is expected, for specific soil moisture conditions and accumulation periods. The FFG system is generally easy to understand and implement, since it does not require advanced calibration methods, thus making it a practical tool for enhancing flash flood warnings in any region [27,33,34]. The quality of the results, however, is still based on the use of weather radar datasets. In the implementation of the system worldwide [27], the system also uses satellite data, but increased effort is still

required to reach the desired accuracy. Nonetheless, the system provides basic warnings in countries that otherwise would have none.

This study aims to further assess the use of weather radar in flash flood hazard assessment by providing a complete framework for implementing the GFFG methodology fused with datasets obtained by an X-Band weather radar, the Rainscanner, stationed at the National Technical University of Athens (NTUA). The proposed methodology incorporates fine-resolution datasets calibrating and configuring rainfall–runoff models to provide fine-resolution flood hazard assessments. The results aim to shed more light on flood hazards in the region of Attica, Greece, which features a complex topography that leads to multiple small-scale urban and peri-urban subbasins prone to flooding. Finally, a series of historical events is simulated, and a sensitivity analysis is performed to assess the system parameters.

2. Study Area and Methods

2.1. Study Area and Data Used

This research focuses on assessing flood hazards applicable in real time using the Rainscanner system installed on the NTUA campus in the Zografou municipality with the city of Athens, Figure 1. The system's location lies on the eastern border of Athens city, at the foothills of Hymettus mountain. The city of Athens is surrounded by mountains, Penteli on the northeast, Parnitha on the northwest, Aigaleo on the west, and Hymettus on the east, while to the south and southwest lies the gulf of Salamina. Beyond Mount Aigaleo lies the west Attica region, which includes the Sarantapotamos River basin, the second largest river basin of the Attica region after the Kifissos River basin, while beyond Mount Hymettus on the southeast lies the Mesogeia region. The west Attica region is characterized by industrial areas near the city of Athens, namely the cities of Aspropirgos, Elefsina, and Mandra, while the rest is considered rural. Although not as populated as the Kifissos River basin area, it is vulnerable to flash floods due to its geomorphological and meteorological properties. Specifically, the area features small but steep river basins that lead to flash floods.

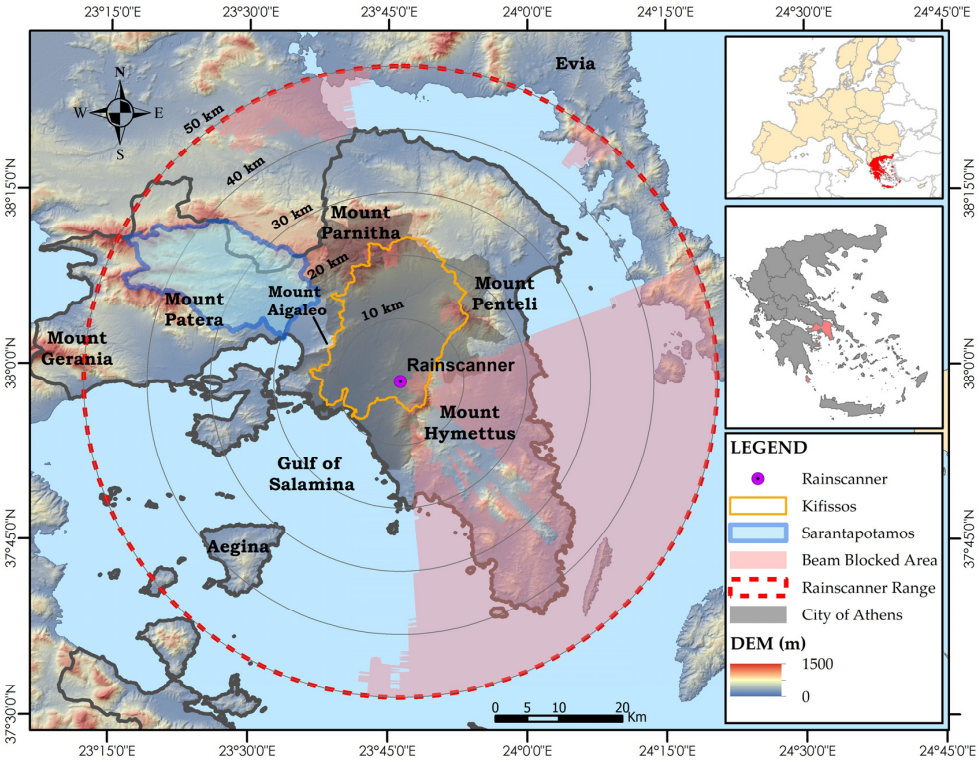


Figure 1. The study area, illustrating the radar range, blockage area, and main subbasins.

Moreover, the area is urbanized on the coastal front, which makes it vulnerable to flash flood events, as observed with the Mandra 2017 flash flood event that resulted in the loss of 24 human lives and severe socioeconomic damage. Finally, recent forest fires between 2021 and 2023 have reduced the available forest quantity, which is crucial for reducing effective rainfall and increasing flood risk. As seen in Figure 2, the areas burned in Attica include the high-elevation regions of the entire West Attica region and the northern part of the Kifissos River basin. This fact significantly impacts rainfall runoff; should the deadly Mandra 2017 flash flood incident re-occur, the estimated flood risk would be higher, and the recent flood-mitigating measures might not be enough to reduce flooding in the designed/expected regions.

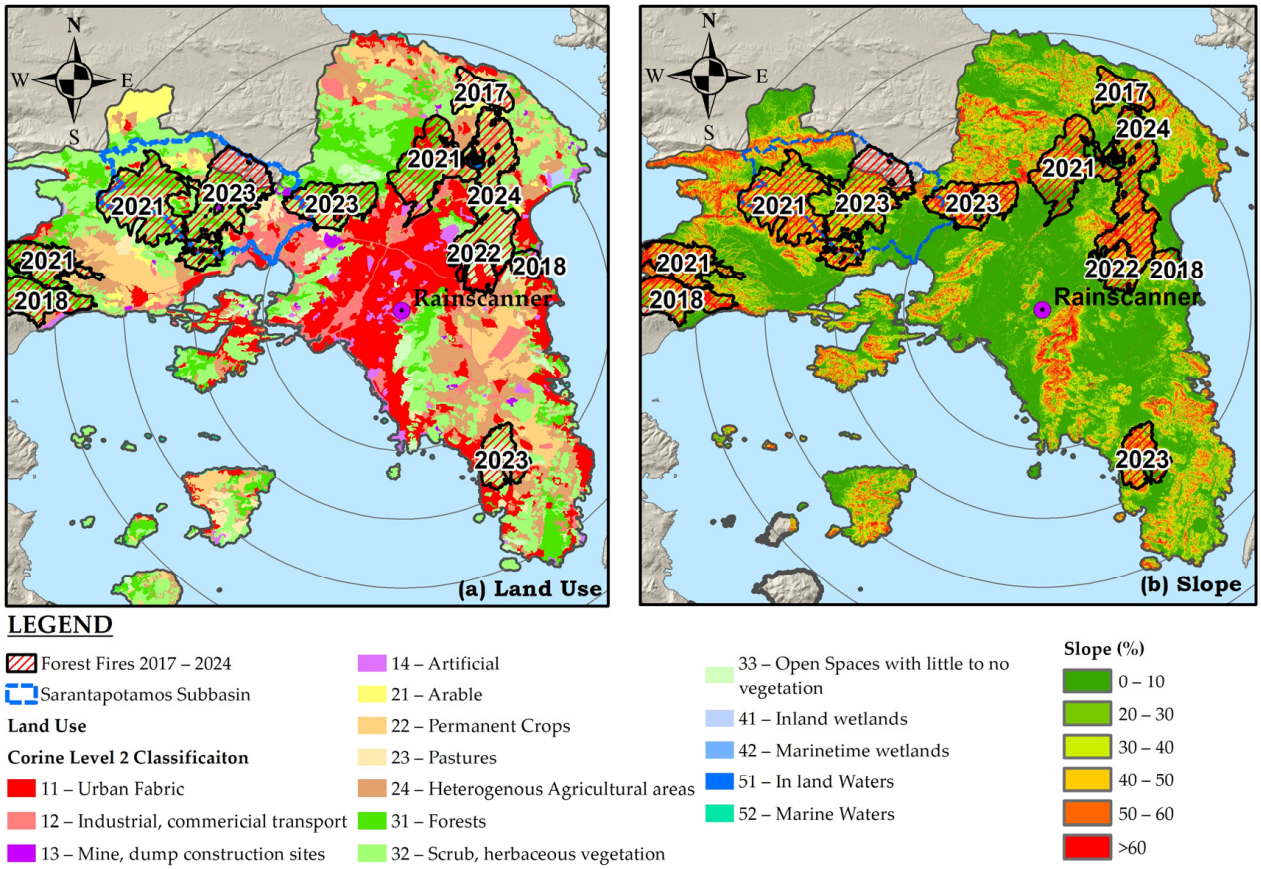


Figure 2. The study area. (**a**) Land use (CORINE 2018) and (**b**) slope (%), along with the areas affected by forest fires during 2017–2024.

From a topographical point of view, the Rainscanner is not in an optimal position to observe the entire Attica region due to its proximity to the mountain Hymettus on the southeast. As seen in Figure 1, this proximity leads to an obstruction of the view to the entire southeast area, which results in considerable data loss. However, it is a known fact, also to be highlighted in this research, that most rainfall fields in the area have a western-to-eastern direction, which suits the Rainscanner position. The system operates at a fixed angle of two degrees, which is set as low as possible to avoid obstacles in central and western Athens, such as the high elevation areas of the Aigaleo, Penteli, and Parnitha mountains, ensuring a clear view to the west, past Aigaleo mountain and over the Saronic Gulf.

In Attica, a large number of small, steep basins are found. The largest is the Kifissos River basin, which is highly urbanized, and the second is the Sarantapotamos River basin, which features rural characteristics in the high elevations and urban characteristics near its outlet. The land use in the rural areas, accounting for 73% of the region, is mainly

agricultural and forest type. However, as mentioned earlier and illustrated in Figure 2, a significant area of mainly forest type has been affected by recent wildfires. This affects the estimated Curve Number (CN) value, which is used to estimate rainfall losses. A burned area usually assumes an increase of 10 to 15 points of CN, which is significant, considering that CN varies from 30 to 100, with the larger values denoting impermeable areas that lead to high runoff potential. Finally, it is also shown in Figure 2 that the areas affected are also the areas featuring high slopes, i.e., the mountainous areas. These findings showcase that the areas affected have become more prone to flash floods.

From the meteorological point of view, the region features only 350–400 mm of average annual rainfall in the lowlands and 1000 mm in the mountainous parts [35]. Since 2008, these figures have seemed to drop, a result attributed to the impact of climate change as less rainfall has been observed in the last decade than previously. Nonetheless, this does not affect the intensity of rainfall events over the region, which has been seen to have risen. Taking into account the Intensity–Duration–Frequency curves constructed for the selected region using datasets up until 2013 and up until 2021, it is evident that more rainfall is expected for the same time period and duration. Nevertheless, the most common type of rainfall systems causing flood generation over the region are the convective-based events, which usually occur either in the early summer or autumn months from September to November. These systems have a typical west-to-east direction; thus, in the west, the Attica region is hit first, increasing the flood vulnerability of the region also due to the lower lead time provided to prepare or warn for possible flood threats.

The Rainscanner system measures rainfall reflectivity on a 100 m $\times$ 100 m per pixel spatial resolution and a 2 min temporal resolution. The system features a 50 km scanning range leading to the generation of a gridded 1000 $\times$ 1000 reflectivity image with the Rainscanner at its center. However, as seen in Figure 1, the southeast area is blocked due to Hymettus Mountain, making it unavailable for scanning. Nevertheless, as mentioned earlier, most storm systems have a west-to-east direction, making the measurements of the Rainscanner system effective for identifying storm systems in time [36]. The system has been operational since 2018, and it is being used for research purposes only. Relevant research work performed by the authors include the Rainscanner datasets quality control procedure [37], aimed to reduce and eliminate errors generated due to ground clutter, as well as filling no-data cells by interpolating nearby cell values under certain constraints, namely, the size of the data loss and its proximity to available data. Finally, the generated datasets are multiple netCDF files, containing the 1000 $\times$ 1000 reflectivity matrix at 2 min temporal resolutions. Each dataset is then processed within MATLAB, v9.13.0 (R2022b), and is assigned an increasing ID number. The system's datasets have been used in numerous research studies by the authors, regarding the calibration and determination of the proper Z–R relationships, i.e., the relationship used to transform the raw reflectivity Z [dBZ] radar measurements into rainfall intensity R [mm/h] [37] and the system's application in rainfall–runoff modeling [26,38] as well as in storm tracking [36]. For more information about the system, the reader is advised to read the above articles.

2.2. Methods

The flood hazard assessment is performed based on the GFFG method. The general flow chart is featured in Figure 3. The key to understanding the entire process lies in threshold runoff and Flash Flood Guidance. Threshold runoff is considered the runoff above which minor flooding occurs. This can be illustrated as the runoff that leads a channel to overflow its banks. By reverse engineering the rainfall runoff process, one can assume that this runoff is generated after a specific amount of rainfall has fallen over the subbasin up to the cross-section. This amount of rainfall is called the Flash Flood

Guidance. However, since only effective rainfall results in runoff, one must consider the volume of rainfall losses. The FFG concept achieves this by evaluating the soil moisture percentage. A high soil moisture percentage leads to fewer rainfall losses and, thus, higher discharge values. Moreover, since the precise name of the FFG is "the rainfall height of a predetermined duration and soil moisture conditions that lead to minor flooding", the durations need to be defined. Since the FFG concept aims to deal with possible flash flood threats, the durations used are periods that are commonly used in nowcasting, namely the 1, 3, and 6 h durations. Multiple durations are justified since the longer the duration, the longer the lead time provided, but with higher forecast uncertainty.

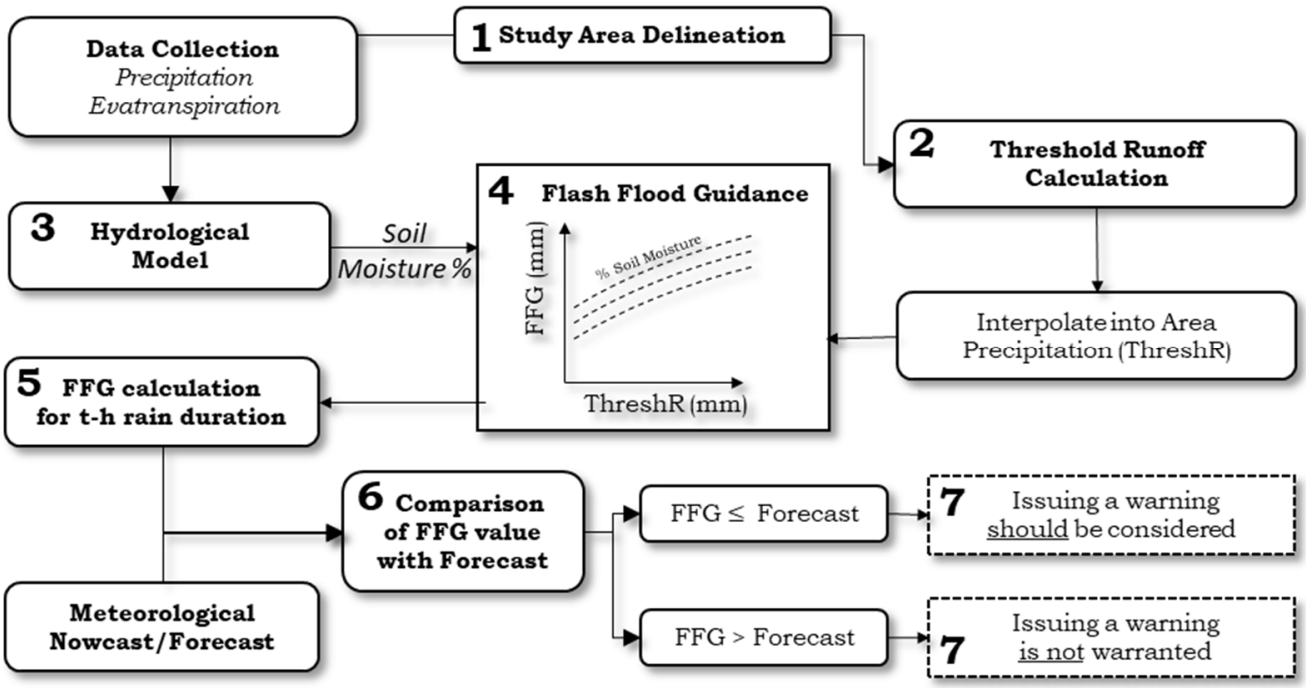


Figure 3. The GFFG implementation flowchart.

The application of the GFFG method relies on offline and online processes. The offline process includes steps 1, 2, and 3 shown in Figure 3, whereas the online process includes steps 5 to 7. First, the study area needs to be delineated into either subbasin, as in the original FFG application, or grids of predetermined size, as in the GFFG implementation. In this implementation, a 0.5 km^2 grid size is selected since it is considered optimal due to the area geomorphology, the subbasin sizes, and the available rainfall forecasting products [39–43]. Smaller grid sizes were deemed hydrologically incorrect based on the rainfall–runoff methods, while larger sizes led to coarser resolutions.

The next step is considered crucial and deals with the estimation of the threshold runoff of each grid. Although the concept explained earlier deals with a cross-section, in the GFFG implementation, this is realized only as the amount of runoff that will cause flooding onto the entire area of the grid. Based on research, minor flooding occurs when the runoff is equal to the 2-year Average Recurrence Interval (ARI), i.e., the 50% Annual Exceedance Probability (AEP) of the discharge [44,45]. However, since runoff measurements are unavailable, to overcome this issue and establish regional relations, the rainfall ARI can be used instead by assuming that the 5-year rainfall ARI leads to the 2-year runoff ARI [13,31,46]. Although this sounds convenient, this value, i.e., the rainfall ARI value, was examined under an uncertainty analysis to determine the impact on the generated thresholds and, consequently, the generated flood indices. The rainfall ARI can be estimated from the IDF curve analysis performed during the river flood management plans developed for Greece. In this study,

the updated IDF, also referred to as ombrian curves [47], were based on point measurements, and a regionalization procedure was undertaken to simultaneously perform a combined estimation of the parameters' values exhibiting spatial and temporal variations based on a Pareto distribution equation governed by five parameters, as follows [48,49],

$$i(d,T) = \lambda \frac{(T/\beta)^{\xi} - 1}{(1 + d/\alpha)^{\eta}} \quad (1)$$

where i [mm/h] is the rainfall intensity, T [years] is the return period, d [h] is the rainfall duration, and λ, β, ξ, α, η are parameters of the equation provided for each grid. In Figure 4, the right subfigure features the rainfall height estimate after the application of Equation (1) for a return period (T) of 5 years and a duration (d) of 3 h.

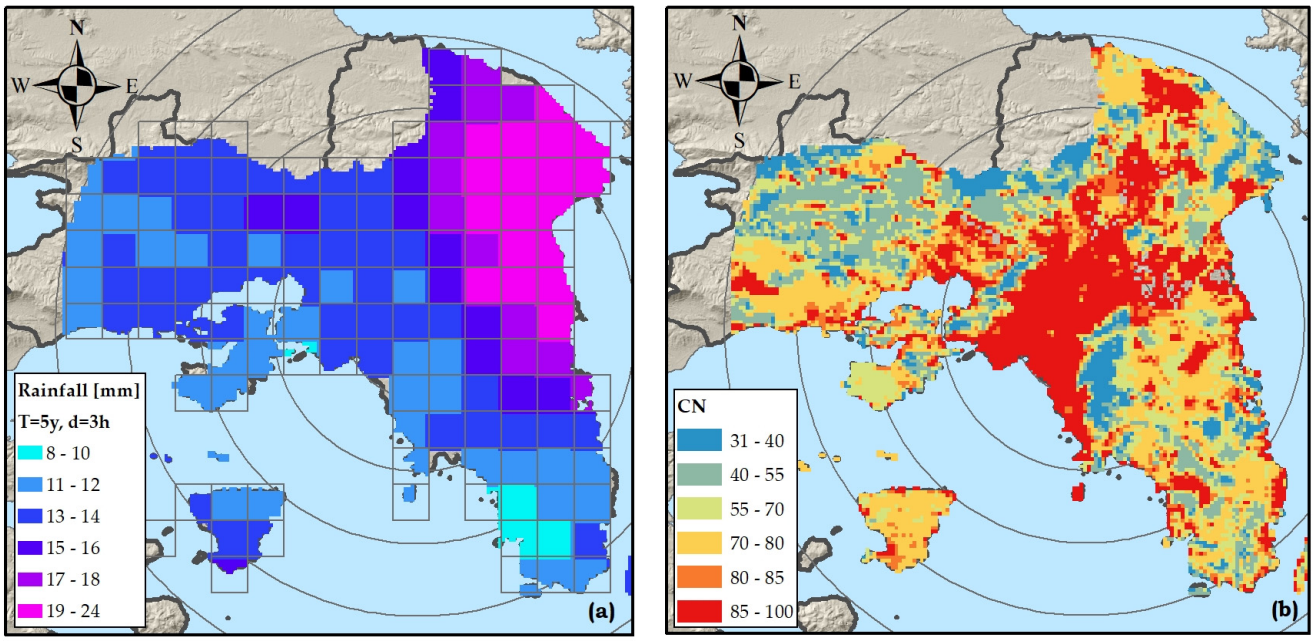


Figure 4. The study area. (**a**) Slope (%) and (**b**) the available IDF grids, illustrating the rainfall height for a return period of 5 years and 3 h duration.

The third instance of the offline mode is the hydrological model. This usually includes a continued simulating rainfall–runoff model to estimate the current soil moisture conditions at each time interval. In this application, the soil moisture conditions are assessed based on the rainfall 5-day Antecedent Precipitation Index (API), which examines the previous 5-day accumulated precipitation. This value is then converted to a percentage (%) of soil moisture, which is used to estimate the current CN. The CN adjustment is performed according to Bournas et al. [13]. Specifically, the soil moisture percentage is used to adjust the CN linearly between dry, medium, and wet conditions. A 0% soil moisture denotes dry conditions and is assigned the CN_I value, whereas 50% and 100% percent denote medium and wet conditions, respectively, and CN_{II} and CN_{III} values are used instead. In between, soil moisture percentages correspond to adjusted CN values calculated through linear regression between the CN_{II} and the CN_I and CN_{III} values, respectively. The CN_I and CN_{III} values are calculated based on the CN_{II} derived earlier using the following well-known equations [50]:

$$CN_I = \frac{4.3CN_{II}}{10 - 0.058 * CN_{II}} \quad (2)$$

$$CN_{III} = \frac{23CN_{II}}{10 - 0.13 * CN_{II}} \quad (3)$$

The CN value is used to calculate the available storage S [mm], which, according to the method, is calculated as follows:

$$S = 25.4\left(\frac{1000}{CN} - 10\right) \tag{4}$$

The rainfall–runoff model applied is a simple unit hydrograph model based on the Triangular NRCS method. First, the lag time of each cell is calculated through Equation (5), the Mockus lag time equation [50], adjusted for use with the metric system. Then, the time to rise (T_R) is calculated from Equation (6) using the desired rainfall duration (D) as 1, 3, or 6 h. Finally, the runoff peak is calculated using Equation (7).

$$t_L = \frac{(3.28L)^{0.8}(S/25.4 + 1)^{0.7}}{1900y^{0.5}} \tag{5}$$

$$T_R = D/2 + t_L \tag{6}$$

$$Q_p = 0.208A/T_R \tag{7}$$

where t_L is the lag time, L [m] is the main stream channel length, S [mm] is the available storage calculated from Equation (2), y [%] is the grid's slope, T_R [h] is the time to rise, D [h] is the rainfall duration, A [Km^2] is the grid's area, and Q_P [m^3/s] is the peak discharge.

The next step is the application of the rainfall–runoff model to estimate the runoff associated with a selected rainfall (P) and initial abstraction (I_α), calculated using the SCS-CN method as follows:

$$Q = \frac{(P - I_a)^2}{(P - I_a) + S} \tag{8}$$

where P [mm] is the rainfall input, I_α [mm] is the initial abstraction, and S [mm] is the available storage. Since the FFG value is the precipitation (P), for known runoff threshold and soil moisture conditions, i.e., S, solving Equation (8) for precipitation (P), yields:

$$FFG_x = P = I_a + \frac{Q_x \pm \sqrt{Q_x^2 + 4Q_x S_{adj}}}{2} \tag{9}$$

where FFG_x is the FFG value for x hours rainfall duration, I_α [mm] is the initial abstraction, S_{adj} [mm] is the available storage calculated from Equation (2) after using the adjusted CN value based on the current soil moisture conditions, and Q_x is the threshold runoff calculated through Equation (7) for the predetermined duration x instead of D used in Equation (6). The initial abstraction is usually considered a factor of the available storage, taken as 20% of S, i.e., 0.2 S. In this research, however, the 0.1 value is used instead on the basis of the work of Baltas et al. [51], who performed an analysis in a subbasin found in Attica. Therefore, Equation (9) turns into

$$FFG_x = 0.1S_{adj} + \frac{Q_x + \sqrt{Q_x^2 + 4Q_x S_{adj}}}{2} \tag{10}$$

In this research, six historical events are examined to assess the flood hazard. Specifically, the observed rainfall values of the Rainscanner are used as the "forecasted" values to assess the system's ability to detect flood hazards. The six events examined are exhibited in Table 1, along with their ID, day of occurrence, and soil moisture percentage as assumed based on the 5-day Antecedent Precipitation Index (API). While it seems that only a few events are examined, the studied events (a) are the ones that featured a high

enough rainfall intensity to trigger floods in multiple areas during the span of the available data from the Rainscanner system, and (b) they featured some diversity in typical rainfall characteristics, mainly in the classification between convective and stratiform and in the seasonal occurrence. Specifically, out of the six studied events, events 31, 48, and 50 featured convective-based characteristics, i.e., small footprint with high rainfall intensity and high cloud movement velocity, while events 6, 21, and 61 featured stratiform-based characteristics, i.e., larger rainfall coverage over the area, with slower movement velocity and mediocre rainfall intensity. This classification also matches the seasonal variability, since rainfall is not frequent in Athens; rainfall events occurring during the winter season, e.g., mainly in November, feature stratiform-based characteristics while events occurring in the summer, mostly in June, feature convective-based characteristics. Moreover, based on previous research performed by the authors regarding the main storm movements and characteristics in the area [36], the rainfall pattern in Athens showcases a distinctive characteristic, with the majority of convective events having a southwest-to-northeast direction, while stratiform events tend to have a northwest-to-east direction. This finding suggests that most rainfall events in Athens feature similar characteristics over time. Therefore, the current findings can be carefully generalized, considering the limitations of awkward, rare rainfall patterns. This study aims to identify flash flood-prone areas, and therefore, extreme rainfall can easily be identified as hazardous, while medium-to-high rainfall intensity is more difficult to assess with current systems. First, the focus is on identifying the properties that lead areas to flood hazard by calculating and analyzing the flood threshold values through the GFFG system.

Table 1. Simulated events and main characteristics.

Event ID	Start Date/Time	Duration (h)	5-Day API (mm)	Mean Area Cumulative Rainfall (mm)
6	17 December 2018 23:40	14.2	13.8	25.8
21	24 November 2019 21:40	10.8	37.0	30.4
31	1 June 2020 14:00	6.0	0.0	20.5
48	9 June 2021 18:00	8.7	0.2	25.0
50	12 June 2021 11:50	7.2	32.0	26.0
61	23 November 2021 17:30	14.2	2.6	26.4

Finally, we assess the GFFG results on the historical events, and we examine the involved uncertainty concerning key parameters of the GFFG systems, mainly (a) the rainfall return period used to extract the threshold runoff of the grids, (b) the soil moisture percentage prior to the event, and (c) the Z–R relationship used to derive the rainfall intensity from the weather radar datasets. The return period parameter tends to affect the threshold runoff values used to determine the FFG value. A higher return period suggests that a higher intensity of rainfall is required to cause a specific grid to flood. As suggested earlier, the 5-year return period is used, while in this analysis, the 2-year and the 10-year periods are applied and assessed. Following this, the initial soil moisture conditions, introduced as soil moisture percentage, are assessed. The rainfall–runoff model shows that this parameter controls the CN value, i.e., the rainfall losses. A higher soil moisture percentage means near-saturated soils, which by default leads to higher runoff, and thus, areas will be prone to flooding. This analysis will assess the impact of the parameter.

Finally, we examine the Z–R relationship used to assess the input uncertainty. Although it is not a core parameter of the system, the GFFG system is usually operated using gridded weather radar and rainfall datasets, which are subject to uncertainty. A weather

radar measures reflectivity, Z [dBZ], and relies on a proper Z–R relationship to transform these values into rainfall intensity, R [mm/h]. It is known, however, that a Z–R relationship is not static, even for a specific radar, but it depends, apart from the location of the radar, on rainfall characteristics such as the rainfall drop size and distribution that are unknown prior to the event. The main results presented in this study use the Z–R relationship $Z = 321R^{1.53}$, which was derived for Athens based on the same Rainscanner data used in this study [37]. We also apply the well-known Marshal and Palmer relationship, $Z = 200R^{1.60}$ [52], which is suited for stratiform-based events, as well as the Summer Deep Convection relationship, $Z = 300R^{1.40}$, which is commonly used with radar systems for convective-based events [53]. Both relationships are featured in other operational FFG systems such as the one operated by the National Weather Service of the USA [27]. Since a Z–R relationship is an exponential equation, the difference in each case is highlighted on the higher values or reflectivity Z [dBZ]. In Table 2, the impact of the Z–R relationship upon the estimated rainfall intensity is shown for various reflectivity values.

Table 2. Reflectivity to rainfall intensity transformation for various Z–R relationships used.

Z [dBZ]	R [mm/h] $Z = 321R^{1.53}$	R [mm/h] $Z = 200R^{1.60}$	R [mm/h] $Z = 300R^{1.40}$	Intensity Description
25	0.99	1.33	1.04	Weak
30	2.10	2.73	2.36	Moderate
35	4.46	5.62	5.38	Strong
40	9.47	11.53	12.24	Strong
45	20.09	23.68	27.86	Very Strong
50	42.63	48.62	63.40	Intensive

The table shows that the main differences arise above the 35 dBZ level, specifically at the 40 dBZ mark. The first and the third equations showcase similar results due to having similar parameter values, whereas the second, the $Z = 200R^{1.60}$, exhibits high intensity over 40 dBZ. This is typical because stratiform events feature lower reflectivity overall, between the 25 and 35 dBZ marks, therefore, stratiform-based equations apply better to these values, whereas convective-based equations apply better to the higher values, i.e., values above 40 dBZ. A stratiform-based equation will overestimate rainfall when used on high reflectivity, whereas a convective-based equation will underestimate the low values [37].

3. Results

3.1. Derivation of Threshold Maps

As mentioned earlier, the spatial analysis of the generated GFFG maps is chosen to be 500 m × 500 m. The first step involves deriving the threshold runoff of each grid. As mentioned, the threshold runoff is estimated based on a 5-year Average Recurrence Interval (ARI) for rainfall. The IDF data available are in a 5 km × 5 km gridded format of their parameters. The threshR value is obtained using a 5-year return period and a predetermined duration of 1, 3, and 6 h, depending on the FFG value it is compared with. Following this, the GFFG grids, which are smaller in size than the IDF grids, are assigned the value based on the IDF grid to which they belong. If, in any case, a GFFG grid falls within two IDF grids, the IDF methodology dictates that the spatial interpolation of the IDF parameters is performed based on the Thiessen polygon method, i.e., based on the percentage of the area that each IDF polygon contributes to the GFFG grid.

Applying the GFFG methodology, the threshR values, i.e., the rainfall threshold values, can be produced based on the threshold runoff values. The results for fixed soil moisture

conditions are presented in Figure 5 for the entire Attica region. Specifically, in Figure 5, the (a), (b), and (c) subplots illustrate the threshR for the 1-, 3-, and 6-h accumulation periods using the AMC-II conditions, whereas subplot (d) illustrates the threshR for the 3-h period when AMC-III, i.e., saturated, conditions are present. These maps indicate the rainfall volume required in each grid cell to trigger minor flooding over a specific period. Close inspection of the maps reveals interesting properties. First, it is important to note that lower threshR values indicate a grid's greater vulnerability to flooding. A lower rainfall threshold means less rain is required to trigger flooding. For instance, a grid with a 20 mm rainfall threshold over 3 h is more prone to flooding than one with a 40 mm/3 h threshold. Therefore, it is vital to identify areas with low threshR values since they indicate high flood vulnerability.

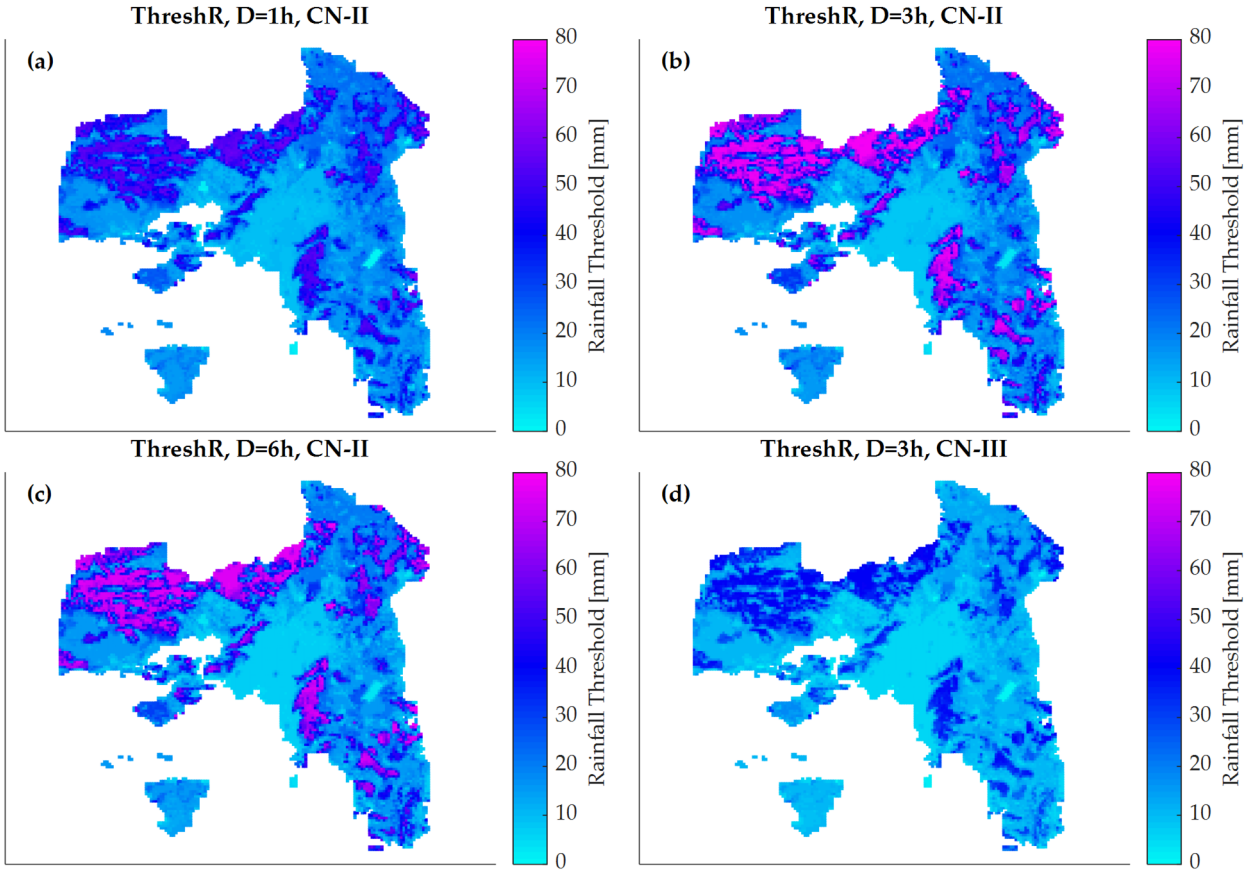


Figure 5. Attica region threshold rainfall under four soil moisture conditions: (**a**) 1 h duration, CN II; (**b**) 3 h duration, CN-II; (**c**) 6 h duration, CN-II; (**d**) 3 h duration, CN-III.

By comparing these low-threshold areas with the CN and slope maps in Figure 4, it becomes clear that lower rainfall thresholds align with regions of high CN values (indicating higher runoff potential) or low slope values. These areas are primarily concentrated within the Athens urban fabric, while in west Attica, they are found in the industrial regions of the southeastern Thriasion plain and in the northern areas, where the flat terrain indicates the location of the Inoi valley.

The boxplots in Figure 6 depict the threshold value distributions for each scenario. Under dry conditions (CN-I), the variability of FFG values across the study area is high, with a range of about 60 mm between the 75th and 25th percentile values across the 3 h and 6 h durations and about 20 mm in the 1 h duration, as illustrated by the first boxes for each duration. However, this variability decreases significantly to 15 mm under normal (CN-II) and 10 mm under fully saturated conditions (CN-III). This finding indicates that

FFG calculation uncertainty is much higher when soil moisture is low. Additionally, the threshold values across all grids tend to decrease as soil moisture increases, but at varying rates. Concerning the median values, illustrated by the red lines in Figure 6, the median values for the 1-, 3-, and 6-h durations are for dry conditions 42, 59, and 61 mm, for normal conditions 25, 30, and 32 mm, and for saturated conditions 16, 17, and 18 mm, respectively.

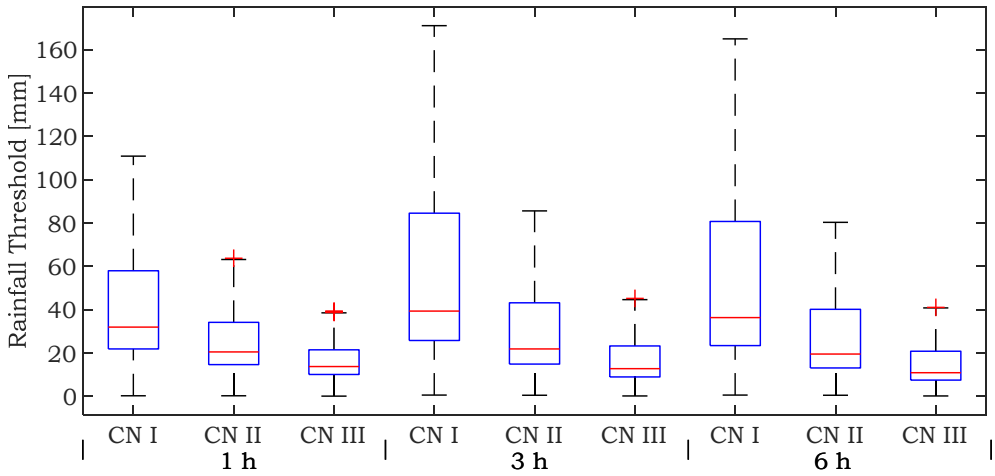


Figure 6. Boxplot of threshold runoff values and different soil moisture conditions for the Attica region. Red lines denote the median value, while the upper and lower boxes limit the 25th and 75th percentiles. Red crosses denote outlier values.

3.2. GFFG for Selected Rainfall Events

This section applies the GFFG model to estimate the flood hazard of historical flood events at a 500 m × 500 m resolution. The rainfall estimates for each event are obtained through the Rainscanner system after applying the $Z = 321R^{1.53}$ Z–R relationship, which was derived from a correlation analysis by Bournas et al. [37], using the Rainscanner datasets and available rain gauge datasets for a series of recorded events. For each event, two sets of maps are presented: the first shows the rainfall over time, while the second displays the GFFG system results, i.e., the cells flagged for flooding. The flooded cells are identified by comparing the GFFG output map with the accumulated rainfall map for the same period; any cell with rainfall exceeding its corresponding FFG threshold is marked as a flooded cell.

Each timestep corresponds to the timestamp displayed on the images, following the Eastern European Time Zone (UTC+2). For example, when the 1 h duration results are shown, the timestamp at 13:00 refers to the accumulated rainfall measured between 12:00 and 13:00. Similarly, the 3 h duration results for the same valid timestamp refer to the accumulated rainfall from 10:00 to 13:00. The advantage of using more extended accumulation periods is that they provide longer lead times. In this application, the observed precipitation from the Rainscanner is the forecasted value; thus, all accumulation periods feature zero uncertainty. However, in real-time conditions, a 6 h precipitation forecast tends to have more uncertainty than the 1 h and 3 h forecasts. To better illustrate the comparison, only the 1 h and 3 h forecast results are used, as most rainfall events last no longer than 10 h, making the 6 h forecasts less practical. Furthermore, after analyzing several events, it becomes clear that long-range forecasts are not feasible due to the velocities of the storms and the limitations of the Rainscanner's range. Extended-duration forecasts would require data from more distant observations.

As described earlier, two different spatial extents are presented in the application area. The first is the Sarantapotamos basin, which provides more detailed rainfall and flood grid results. The second covers the entire Attica region, offering a broader view of the system's

application. However, caution is advised when interpreting the results for the Attica region, as the impact of a sewer system, particularly in highly urbanized areas like Athens, has not been considered. Following this, three events are presented, each characterized by significant rainfall that triggered the GFFG system.

3.2.1. Event 50

The first event analyzed is Event E50, which occurred on 12-06-2021. The results for the entire Attica region are shown in Figure 7, which presents the 3 h rainfall fields and the corresponding flooded cells for each timestep. While the image scale does not allow for the extraction of high-resolution details, it effectively highlights the spatial characteristics of the rainfall.

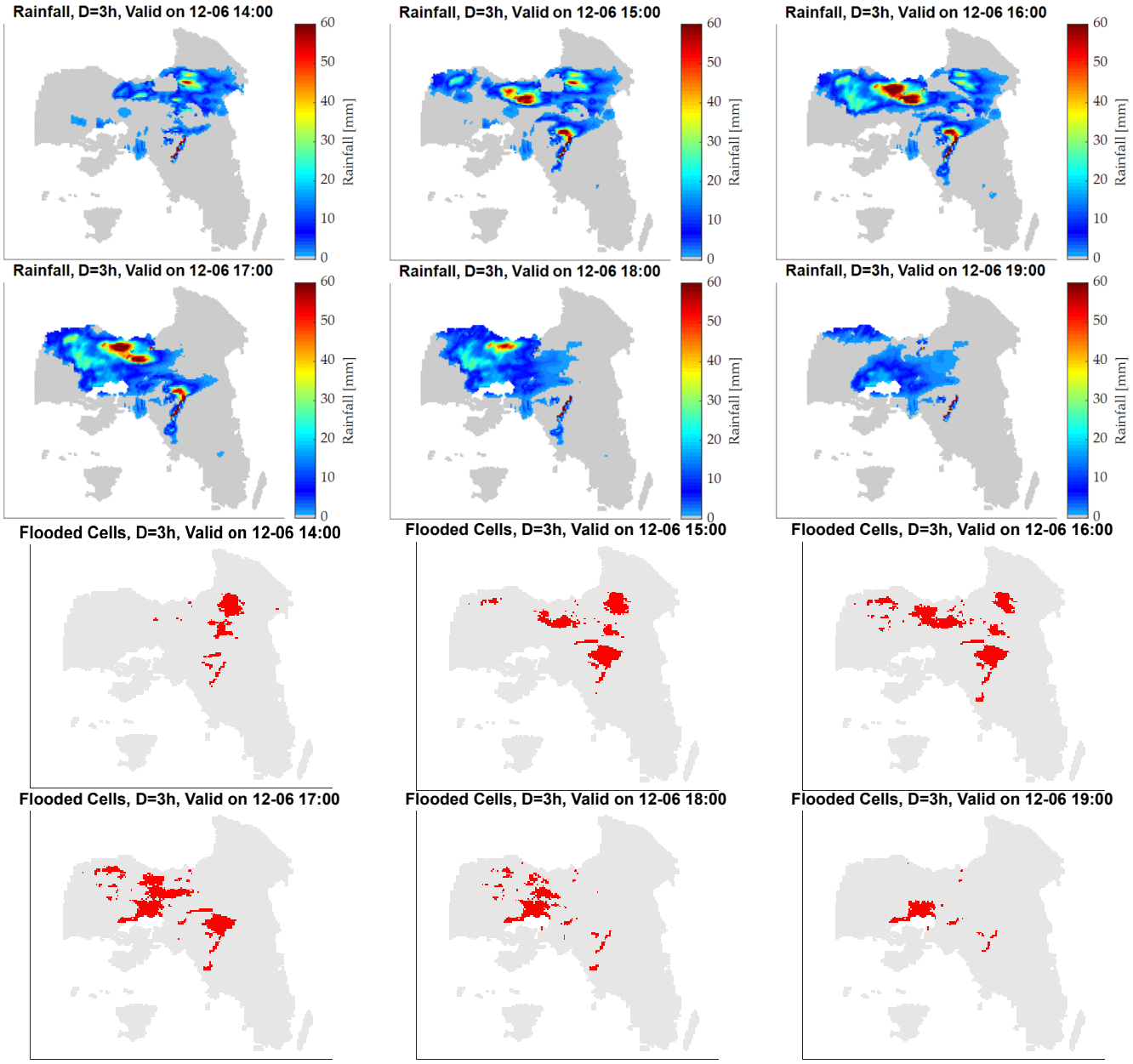


Figure 7. Depictions of 3 h gridded rainfall (**upper**, six frames) and the corresponding flooded cells (**lower** six frames), valid per timestamp for Event 50, in the Attica region. Each rainfall image corresponds to the specific flood hazard map, where the cells that are flooded are illustrated with red color.

This event is distinguished by its small spatial footprint and high rainfall intensities. It is a convective-based event, with visible storm cores identifiable, leading to multiple areas where flooding is anticipated, particularly in high-rainfall regions at various timesteps. Flooding is expected in the northern parts of Attica, such as the foothills of Penteli Mountain, while in the later stages, the storm shifts its focus to western Attica. To better visualize the variability, Figure 8 shows the Sarantapotamos precipitation grid and flooded cells for the 1 h rainfall, while Figure 9 shows the images of the 3 h accumulated period.

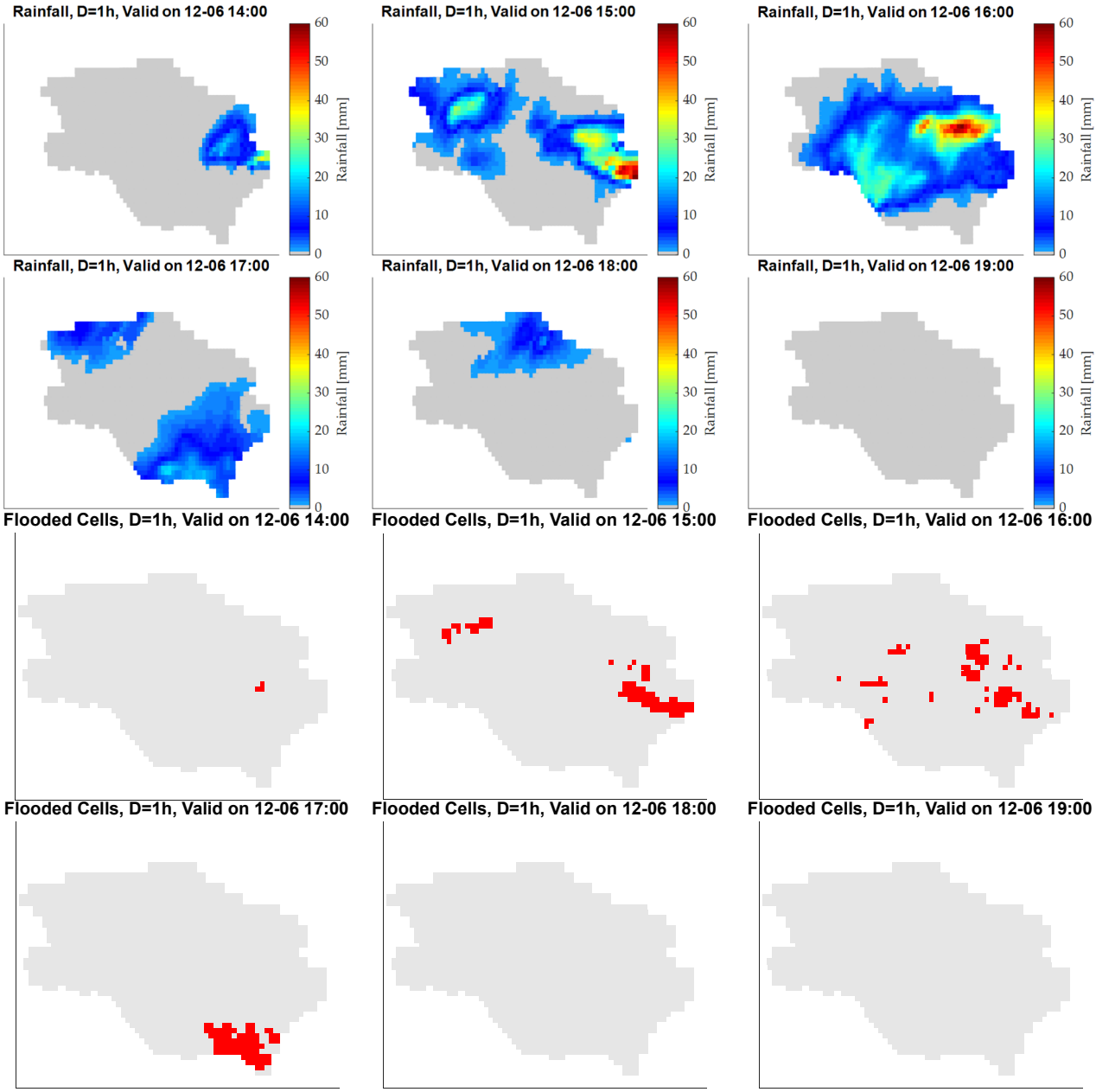


Figure 8. Depiction of 1 h gridded rainfall (**upper**, six frames) and the corresponding flooded cells (**lower** six frames), valid per timestamp for Event 50, for the Sarantapotamos basin. Each rainfall image corresponds to the specific flood hazard map, where the cells that are flooded are illustrated with red color.

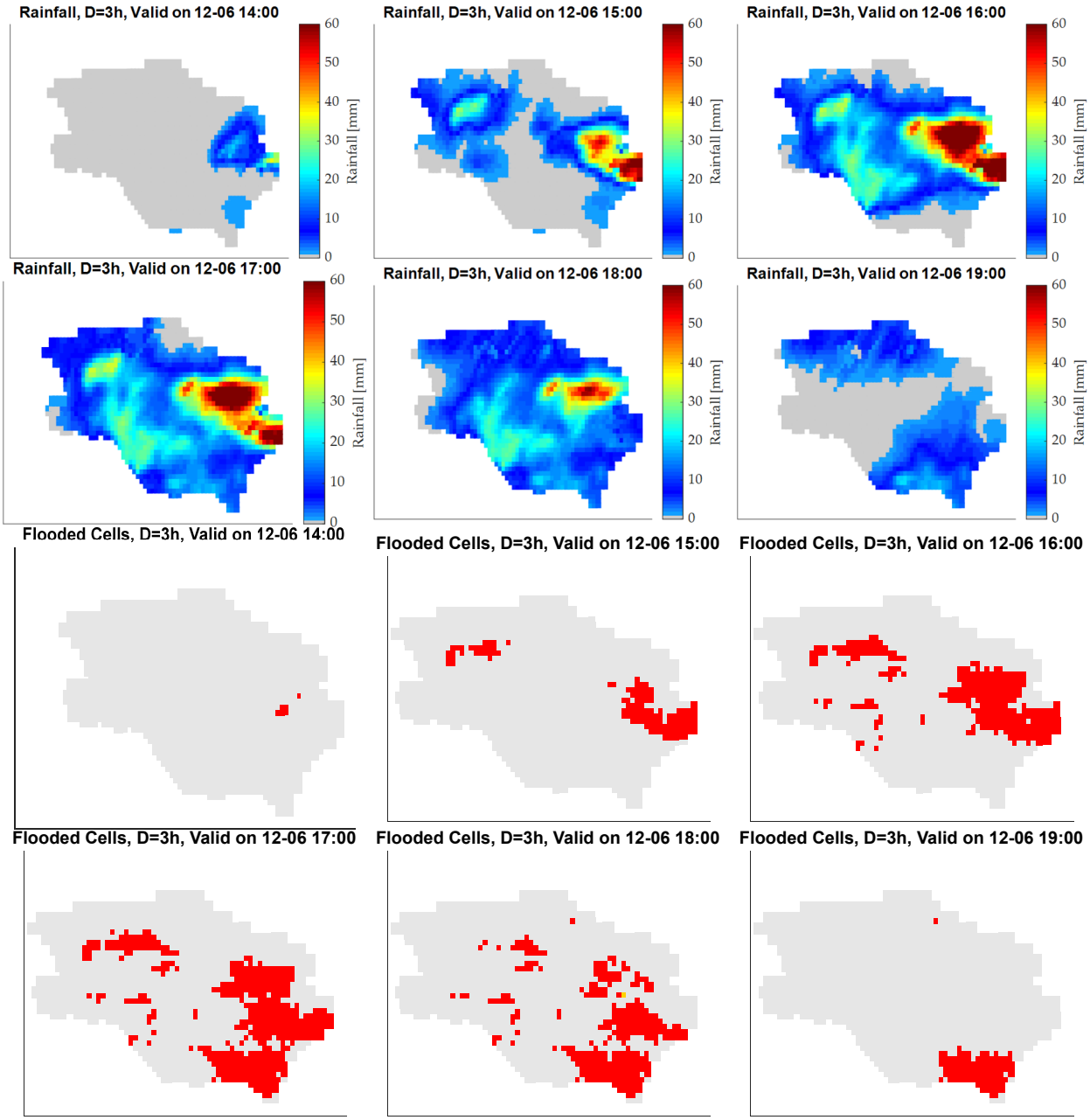


Figure 9. Depiction of 3 h gridded rainfall (**upper**, six frames) and the corresponding flooded cells (**lower** six frames), valid per timestamp for Event 50, for the Sarantapotamos basin. Each rainfall image corresponds to the specific flood hazard map, where the cells that are flooded are illustrated with red color.

The difference between the accumulation periods is evident in the rainfall intensity and the extent of flooding at each timestep. The 3 h accumulation period shows higher rainfall amounts and broader spatial coverage than the 1 h. One advantage of the 3 h products is that they allow for earlier flooding detection. For example, the 1 h precipitation maps indicate that most of the rainfall occurs at the valid time of 15:00, covering the period from 14:00 to 15:00.

In the 1 h products, flooded cells are reported across different timesteps. Initially, the western part is flagged for flooding at the 15:00 and 16:00 timesteps, while at 17:00, only the southern part is flooded. In contrast, the 3 h product illustrated in Figure 9 shows the same areas flooding but at different times. Specifically, the 16:00 timestep includes the accumulated rainfall from 14:00 to 16:00, while the 17:00 timestep covers the period from

15:00 to 17:00, during which most of the rainfall occurred. As a result, the 17:00 timestep shows the most flooded cells, which is the combined total of all flooded cells of the 1 h product from the 15:00, 16:00, and 17:00 timesteps.

3.2.2. Event 31

The second event analyzed is Event E31, which occurred on 01-06-2020. Figure 10 displays the 3 h rainfall fields and the estimated flooded cells for the Attica region. This event is characterized by a small spatial footprint and high rainfall intensities, as highlighted by the visible storm cores. Initially, flooding is predicted in the northern parts of Attica, such as the foothills of Penteli Mountain, while in later phases, the storm shifts its focus to western Attica. Compared with Event E50, rainfall intensity is lower, but the flooding hazard is primarily identified in the west Attica urbanized areas.

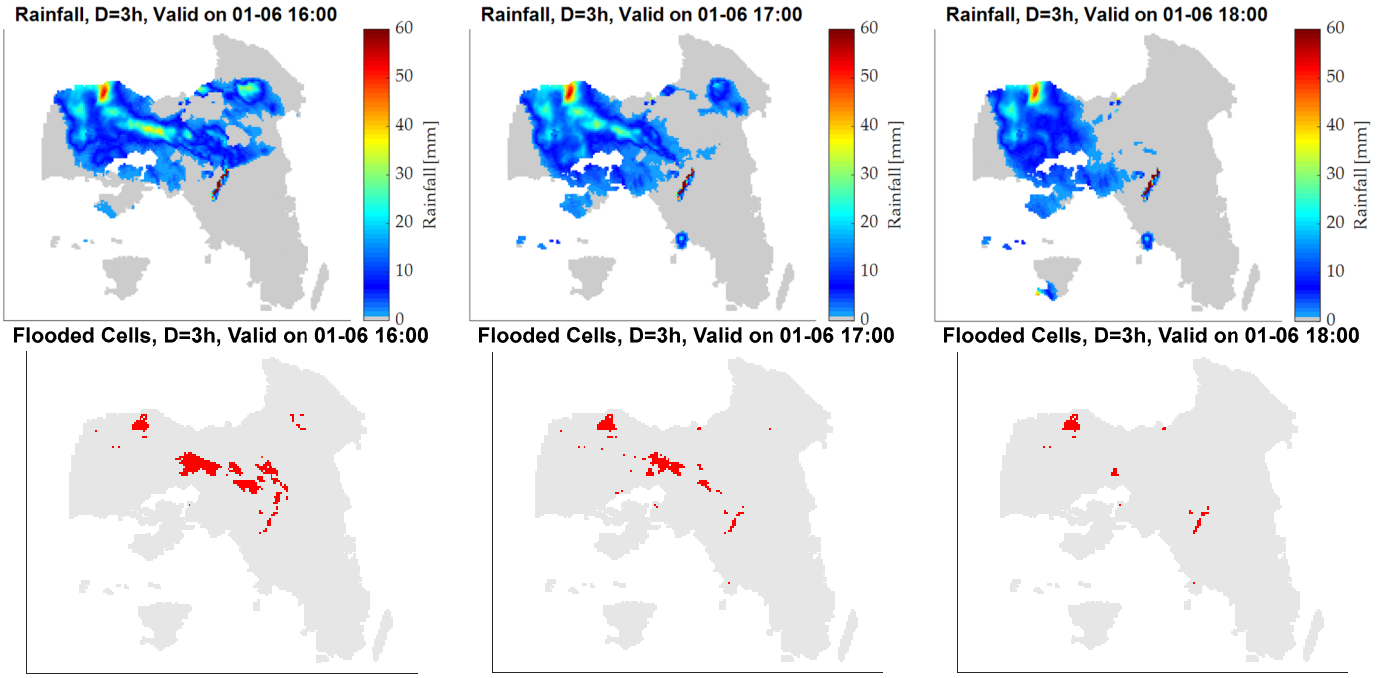


Figure 10. The 3 h gridded rainfall and flooded cells. Result is valid per timestamp for Event 31, at Attica region. Red cells denote cells in which rainfall is over the FFG value.

The critical difference between Events E31 and E50 lies in the soil moisture conditions. For Event E50, soil moisture is identified at 70%, while in Event E31, it is estimated to be at near-dry conditions based on the accumulated rainfall that occurred five days before the event.

3.2.3. Event 21

The third event analyzed is Event E21, which occurred on 25-11-2019. Figure 11 displays the 3 h rainfall fields and the corresponding flooded cells for the Attica region. This event is characterized by a large spatial footprint and moderate rainfall intensities, indicating a stratiform-based event. However, since the rainfall occurred in November, and a significant amount of rain had fallen in the preceding days, the soil moisture conditions were set to near saturation (90%), resulting in a high runoff potential. The flooded cells follow the storm's path, moving west to east. Although many cells are flagged for flooding during this event, the interesting aspect is the progression of flooding, which demonstrates the system's capability to identify when each area is expected to flood or approach flooding conditions.

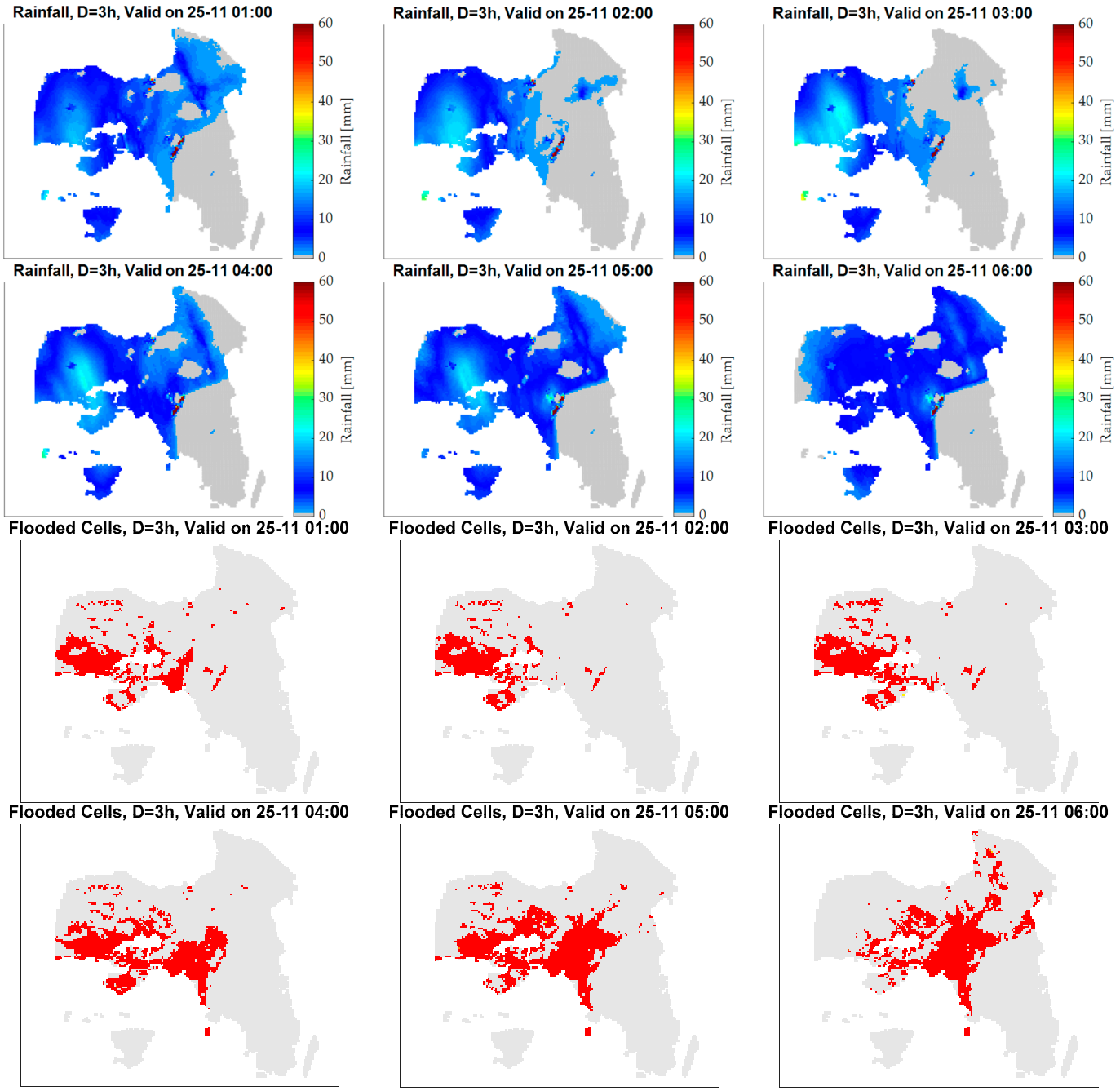


Figure 11. Maps of 3 h gridded rainfall and flooded cells result, valid per timestamp for Event 31, at Sarantapotamos basin. Red cells denote cells in which rainfall is over the FFG value.

3.3. Sensitivity Analysis

The sensitivity analysis examines the impact of varying key parameters in the GFFG system, such as soil moisture conditions and threshold runoff. The system parameters examined are (a) the initial soil moisture conditions, (b) the rainfall return period used to estimate the threshold runoff of each grid, and (c) the Rainscanner Z–R relationship used to turn radar reflectivity into rainfall intensity.

Figure 12 illustrates the effect of each parameter on the 17:00 valid time of the 3 h duration GFFG map of Event 50. The rainfall spatial coverage is illustrated in the first frame of the third row of Figure 7. This frame exhibits high and low rainfall intensity with a selective footprint, making it suitable to visualize any uncertainty results. The first row of Figure 12 illustrates when different soil moisture conditions, 30%, 50%, and 90%, are

used, the second row illustrates when different return periods (T), 2, 5, and 10 years, are applied for threshold runoff, and the third row when different Z–R relationships are used for the weather data, as mentioned in the Methods section and exhibited in the title of each frame. For each case, the percentage of the entire area, i.e., the Attica region, is also shown, leading to a quantitative comparison of the generated results. Since the featured grids are 500 m × 500 m, equal to 0.25 km^2, and the entire area consists of 11,707 cells, 1% results in nearly 30 km^2 covered area.

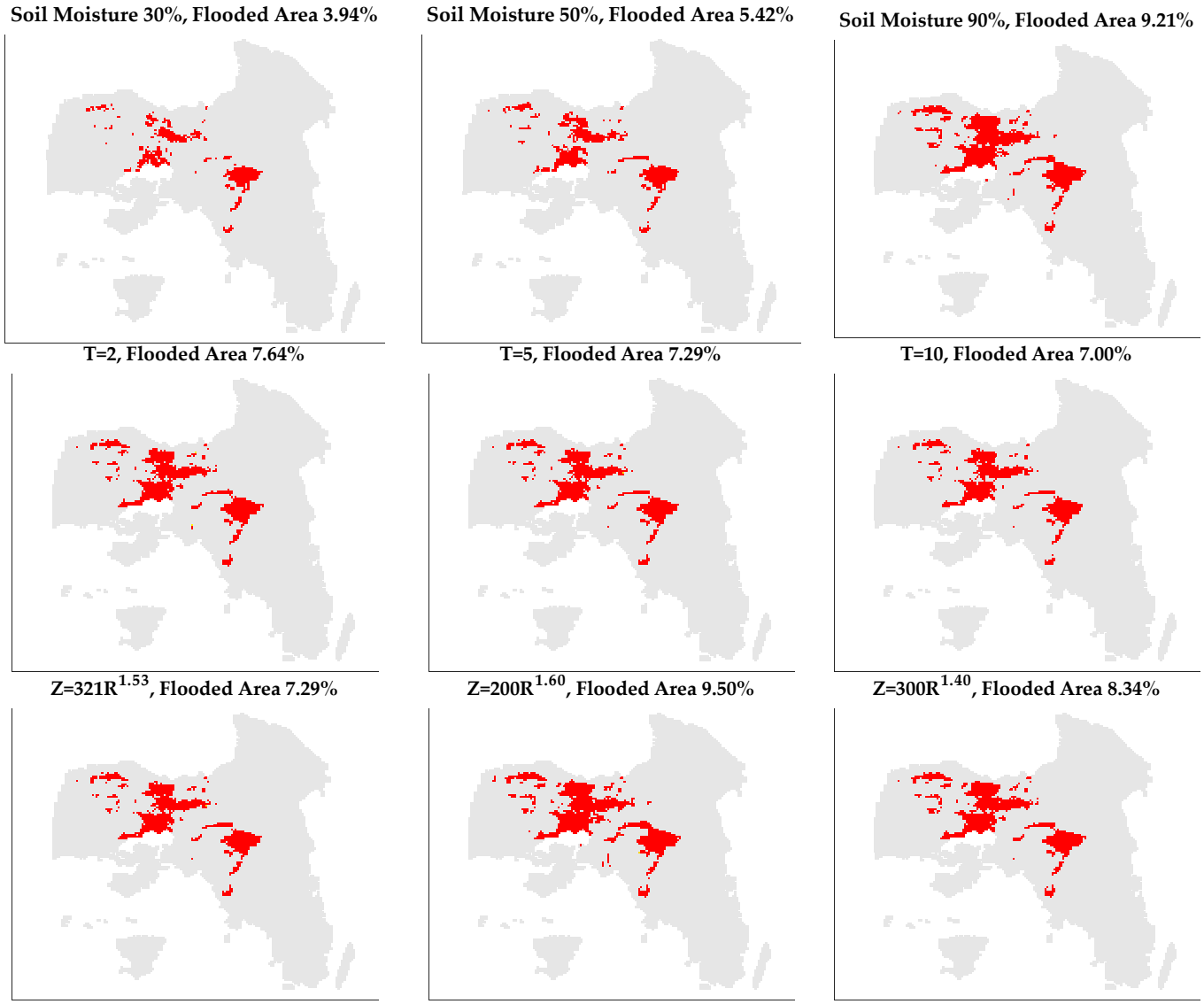


Figure 12. Sensitivity analysis results are shown on the 3 h duration flood map at a valid time of 17:00 for Event 50. Each row illustrates the difference in the flood extent when different parameter values are shown: First row illustrates the difference when different soil moisture conditions are used, the second row when a different return period is applied for threshold runoff, and the third row when different Z–R relationships are used for the weather data. The parameter values and flooded area coverage percentage are illustrated on each subfigure.

As the results show, the soil moisture percentage change significantly changes the total area flagged for flooding. As expected, the higher the soil moisture conditions, the higher the flooded area. Specifically, by utilizing 30% soil moisture, i.e., soils being near dry, only 3.94% is flagged for floods, while for 90% soil moisture, this percentage changes to 9.21%, which is a 5.26% increase, i.e., 157 km^2 more area flagged for flooding. By assuming

medium conditions, 50%, a 5.42% area is covered, roughly 110 km^2 less than in saturated conditions. Overall, it seems that for 10% more soil moisture, approximately 0.90% of the area is covered. Of course, this is subject to the rainfall coverage and rainfall heights. As suggested previously, intensive rainfall will most likely lead to the system flagging the majority of cells for flood since the system aims to identify flash floods, which are defined as minor flooding overland.

Following this, we assess the results of the return period. As mentioned, the return period is used in conjunction with the IDF curves to assist in defining the runoff thresholds of the grids. Assuming a 5-year return period as the threshold, we assume that any rainfall featuring a higher return period will possibly cause flooding, subject to the grid's slope, land cover, and initial soil moisture conditions. Therefore, we assess whether this selection is crucial to the generated results. In the second row of Figure 12, it is visible that changes to the return period did not lead to substantial changes to the flooded area. As expected, a lower return period suggests that the grids are more prone to flooding, but the margin is insignificant. Even when 10 years is used, only a 0.29% decrease in flooded area is featured.

Finally, we examine the Z–R relationships used to assess rainfall input. As mentioned earlier, the first relationship, $Z = 321R^{1.53}$, fits both stratiform and convective events, whereas the $Z = 200R^{1.60}$ focuses on stratiform and the $Z = 300R^{1.40}$ on solely convective. The results show that there can be some impact on the generated results, with roughly a one percent difference, i.e., 30 km^2 of calculated flooded space, between the relationships. The $Z = 200R^{1.60}$ relationship features the higher flood area, while the $Z = 321R^{1.53}$ is the least. Considering the effect of Z–R in the rainfall intensity, as shown in Table 2, the higher differences appear in the higher reflectivity values. Therefore, the results are roughly anticipated since Event 50 is a convective-based event featuring high reflectivity values, and therefore, applying a stratiform-based relationship will most likely overestimate the rainfall intensity. When comparing the other two relationship results, minor differences are observed in the flood extent, assuming that the added cells flagged for flooding are cells near already flooded cells. Rainfall is the driving force of runoff, and it is expected to impact the generated results. These results show the importance of calibrating the weather radar rainfall systems with a proper Z–R relationship. Moreover, they show that rainfall datasets that are subject to increased uncertainty, such as raw satellite measurements or not dense rain gauge networks, will mostly likely lead to unrealistic flood maps.

Overall, it is shown that soil moisture conditions are the most crucial parameters, highlighting the need to better simulate and assess these conditions prior to a flash flood event.

4. Discussion

Figure 13 presents the system's results concerning the total grids flagged for flooding for all the studied events featured in Table 1 across all accumulation durations for the Attica region. Moreover, in the featured maps, the color bars indicate the frequency with which each grid was flagged for the specific event. Specifically, grids with red to purple colors indicate that they were flagged for flooding for the majority of the events' duration, i.e., over 50%, whereas grids with yellow coloring indicate that only for a few instances did the rainfall overcome the threshold, resulting in minor flooding. However, it should be noted that a grid being flagged for flooding is still counted as a flooded grid, meaning that flood hazard occurs on the specific cell. Nonetheless, this distinction assists in identifying the grids that were affected by the storm the longest, meaning that aside from uncertainty, they are prone to excessive flooding.

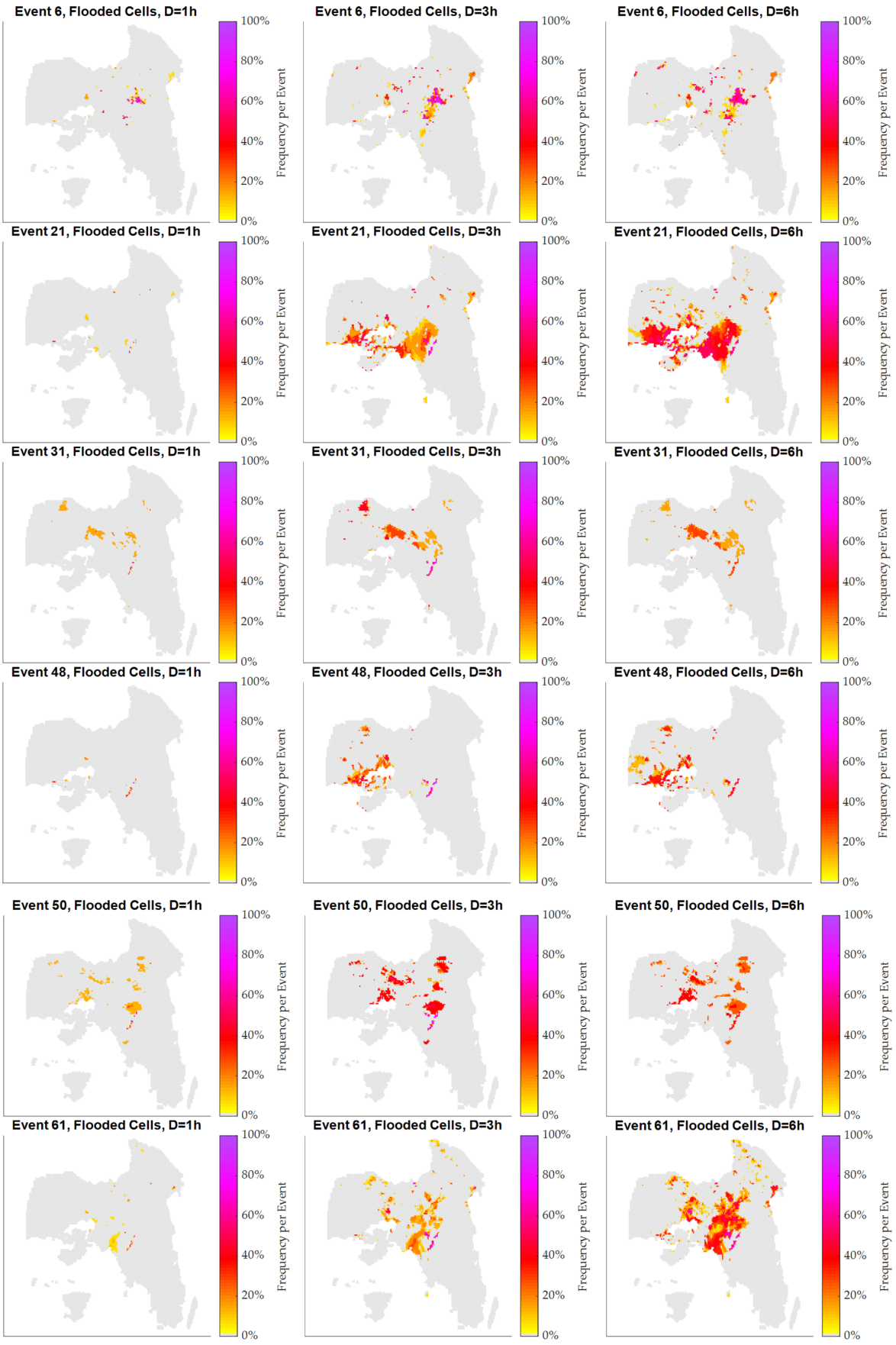


Figure 13. Cells flagged for flood during the entire duration of each event for each of the accumulation period products; first column 1 h, second column 3 h, and third column 6 h. The color bars denote the percentage of time that each grid was flagged for flooding.

The maps indicate that most of the cells flagged for flooding are typically located in urban areas, particularly in the Athens metropolitan region. Specifically, two events, Events 21 and 61, seem to affect the center of Athens, while the rest of events affect the north and northwestern suburbs of Athens. In either case, most of the time, the results of the 3 h and 6 h are near-identical, while in some cases, the 1 h results flag fewer grids than the respective 3 and 6 h products. This can be attributed to the fact that rainfall often occurs at high intensity for only a few moments. Therefore, the 3 h and 6 h products that included this period illustrated flooding cells. This fact highlights that, at least in Athens, intense rainfall has a limited duration of even less than an hour, making nowcast and flood forecasting challenging on high temporal scales.

The 3 h nowcast seems to provide adequate information regarding the affected areas. The only issue with more extensive accumulation periods is that the exact time and place of flooding within the period is unknown. In a 3 h forecast, flooding might occur in the first or third hours. To that end, examining the lower accumulation period results, e.g., the 1 h product, is necessary to correctly assess the current and forecasted conditions.

However, as previously discussed, the system does not account for the influence of sewer systems, meaning the flagged cells may not necessarily have led to actual flooding. This can be achieved by identifying the areas where a sewer network exists and increasing the rainfall thresholds. One easy-to-implement idea assumes that a typical sewer network is designed for a 10- to 20-year rainfall return period, thus increasing the rainfall return period for flooding from the previously used 5-year to over 20 years. Moreover, considering that (a) sewer entry points are often clogged with sediments and (b) the sewer networks were designed in the past, making them under-designed for current climate conditions, one can assume that they offer a 10-year rainfall return period safety. However, as shown earlier, the impact of the rainfall return period is not as crucial in these scales, assuming that even a few centimeters of water flowing over the streets can be dangerous or even fatal in some cases. Furthermore, at considerable rainfall-intensive events, sewer systems are usually so clogged that streets turn into rivers, as seen in the cases of the Mandra event in 2017 as well as the most recent one in November 2024 in Valencia, Spain, where, based on current information, more than 200 human lives were lost due to flash flooding.

Regarding the impact of system parameters on the results, most parameters have a noticeable effect only when the expected rainfall is close to or exceeds the calculated threshold. However, flooding is almost always predicted when the rainfall significantly surpasses the threshold. Soil moisture conditions have a more significant influence than the selected rainfall return period when calculating threshold runoff. This is demonstrated in the simulation of Event E21, where although lower rainfall amounts were recorded, a higher number of cells was flagged for flooding due to the near-saturated soil conditions considering the rainfall accumulated over the preceding five days.

Another critical observation is that, in most cases, the different accumulation periods produced similar results regarding the total number of flooded cells. Exceptions were noted in Events E6, E48, and E61, where the 3 h and 6 h durations resulted in significantly more flooded cells than the 1 h duration. This can be attributed to the stricter 1 h thresholds and the rainfall amounts being either just below or above the threshold. This highlights the importance of using multi-duration products, as they provide a more comprehensive understanding and assessment of flood risk. Finally, rather than relying solely on a deterministic "flood or no flood" result, the flood risk can be quantified by calculating the difference between the rainfall height and the threshold value, indicating the severity of the expected flood. In this context, an appropriate decision-making strategy should be implemented to determine whether a flood warning should be issued.

Overall, it is possible to analyze the parameters that can be examined further and enhance the system with more detail. However, no matter the detail of each component studied and simulated, in early warning systems focused on flash floods, three key points need to be addressed. The first is the structure of the warning system. Due to the nature of flash floods, a flash flood EWS should primarily focus on assessing rainfall thresholds rather than stage or streamflow thresholds. Although this might not lead to detailed information regarding the exact time and place where flooding occurs, available after hydraulic simulations, it allows for adequate lead times, deemed crucial when dealing with such events.

The second key point is the rainfall input. To that end, the remote sensed rainfall input is mainly from weather radars such as X-Band. Weather radars that offer high spatial and temporal resolutions can enhance current forecasting and nowcasting abilities to provide extended lead times. This is exhibited by the minimal, if any, difference when comparing the 6 h rainfall accumulation period with the smaller ones. Nonetheless, a 3 h lead time in the case of Athens and Attica is expected to provide adequate time to inform people and act accordingly. Currently, in Greece, the "112" warning system is based on meteorological forecasts that lack spatial precision, leading to people losing trust when warnings are issued in areas where not even intense rainfall is observed.

The third crucial parameter is the rainfall–runoff transformation. A flash flood is characterized by the quick response of a subbasin, and to that end, the initial conditions and basin topography are of great importance. Both these subjects are included in the system, the first by assuming a soil moisture percentage as the input to estimate the adjustment in the CN values and the second by incorporating a rainfall–runoff transformation that includes the slope parameter. In any case, this component requires a reassessment should the area of land use be changed, either in the form of urban expansion or, as recently, due to forest fires, reducing the rainfall losses; thus, the CN is changed. As shown in the sensitivity analysis, this parameter is considered more crucial than the rainfall return period used to assess the threshold, denoting that even though climate change is expected to increase the intensity of storm events, the generated runoff in flash floods is more dependent upon "static" factors, namely, the slope and the permeability of the area onto which rain falls.

All the above factors are included in the GFFG system. The critical flood hazard assessment is illustrated in Figure 5, where the thresholds for medium saturated conditions are shown. Such maps can be easily generated should different soil moisture conditions be present.

5. Conclusions

In this study, the GFFG system was implemented for use in both rural basins, such as the Sarantapotamos River basin, and larger regions covered by the radar system, namely, the entire Attica region. The system is based on the FFG concept, where the crucial rainfall value is estimated as a rainfall threshold, the FFG value, above which flooding is expected. A key improvement in this research is the gridded approach to the FFG system in the GFFG system, where all calculations, parameters, and variables are analyzed on a grid rather than in subbasin units. This enhances the system's flexibility, as it can adjust to various grid sizes based on rainfall forecast scale, allowing for better spatial and temporal resolution. The system consists of four main components: (a) threshold runoff derivation, (b) current soil moisture conditions, (c) FFG value calculation, and (d) comparison of forecasted values with FFG values. The most critical components identified are the threshold runoff and the soil moisture conditions. The threshold maps generated illustrate two main findings. Flood hazards are anticipated in areas with high imperviousness and low slopes, as illustrated by the low FFG values calculated, which denote that less rainfall is required for a specific

grid to flood. Soil moisture conditions significantly affect permeable land covers since the CN value changes considerably between dry and wet conditions, while impervious areas, e.g., the urban areas, which already have a high runoff potential, are less dependent on soil moisture conditions.

The system was applied to six events, calculating the FFG values for three predetermined accumulation durations (1, 3, and 6 h) and soil moisture conditions. Interpreting the different accumulation periods is crucial, as shorter durations provide smaller lead times but with less uncertainty. In comparison, longer durations offer more significant lead times but with increased uncertainty due to both forecast uncertainty and the variability in the exact timing of flooding within the period. Most areas flagged for flooding were urban areas with high CN values, followed by areas with high slopes.

The system performed as expected in all events, accurately reflecting the rainfall field for each case. Ultimately, the most significant factors influencing the system's performance are the soil moisture conditions before the event and the amount of rainfall occurring over a given grid. Both cases can be acquired through remotely sensed datasets using high-resolution X-Band weather radar or satellite images. Future work will focus on the assessment of soil moisture conditions from satellite images as well as the assessment of the system in real-time conditions using forecasted rainfall fields. A limitation of the study is the unavailability of in situ or satellite datasets to validate the generated results. However, ongoing monitoring of new events, should they occur, will be sought to be validated with such data. Finally, fuzzy logic can also be examined and incorporated into the system to assess when a grid should be flagged as flooded, since a deterministic threshold is not ideal when the rainfall values are near the calculated FFG value.

Author Contributions: Conceptualization, A.B. and E.B.; methods, A.B.; software, A.B.; validation, A.B. and E.B.; formal analysis, A.B.; investigation, A.B.; resources, A.B. and E.B.; data curation, A.B.; writing—original draft preparation, A.B.; writing—review and editing, A.B. and E.B.; visualization, A.B.; supervision, E.B.; project administration, E.B.; funding acquisition, A.B. All authors have read and agreed to the published version of the manuscript.

Funding: This research received no external funding.

Data Availability Statement: The data that support the findings of this study may be available from the corresponding author upon reasonable request.

Conflicts of Interest: The authors declare no conflicts of interest.

References

1. Blöschl, G.; Hall, J.; Viglione, A.; Perdigão, R.A.; Parajka, J.; Merz, B.; Lun, D.; Arheimer, B.; Aronica, G.T.; Bilibashi, A. Changing Climate Both Increases and Decreases European River Floods. *Nature* **2019**, *573*, 108–111. [CrossRef] [PubMed]
2. Diakakis, M.; Andreadakis, E.; Nikolopoulos, E.I.; Spyrou, N.I.; Gogou, M.E.; Deligiannakis, G.; Katsetsiadou, N.K.; Antoniadis, Z.; Melaki, M.; Georgakopoulos, A.; et al. An Integrated Approach of Ground and Aerial Observations in Flash Flood Disaster Investigations. The Case of the 2017 Mandra Flash Flood in Greece. *Int. J. Disaster Risk Reduct.* **2019**, *33*, 290–309. [CrossRef]
3. Spyrou, C.; Varlas, G.; Pappa, A.; Mentzafou, A.; Katsafados, P.; Papadopoulos, A.; Anagnostou, M.N.; Kalogiros, J. Implementation of a Nowcasting Hydrometeorological System for Studying Flash Flood Events: The Case of Mandra, Greece. *Remote Sens.* **2020**, *12*, 2784. [CrossRef]
4. Feloni, E.; Theochari, A.P.; Skroufouta, S.; Bournas, A.; Baltas, E. Analysis of the Hydrologic Conditions during the Flood Event Occurred in Mandra, Greece, on November 2017. In Proceedings of the International Conference on Environmental Science and Technology (CEST), Athens, Greece, 1–4 September 2021.
5. Diakakis, M.; Mavroulis, S.; Deligiannakis, G. Floods in Greece, a Statistical and Spatial Approach. *Nat. Hazards* **2012**, *62*, 485–500. [CrossRef]
6. Pereira, S.; Diakakis, M.; Deligiannakis, G.; Zêzere, J.L. Comparing Flood Mortality in Portugal and Greece (Western and Eastern Mediterranean). *Int. J. Disaster Risk Reduct.* **2017**, *22*, 147–157. [CrossRef]

7. Varlas, G.; Anagnostou, M.N.; Spyrou, C.; Papadopoulos, A.; Kalogiros, J.; Mentzafou, A.; Michaelides, S.; Baltas, E.; Karymbalis, E.; Katsafados, P. A Multi-Platform Hydrometeorological Analysis of the Flash Flood Event of 15 November 2017 in Attica, Greece. *Remote Sens.* **2019**, *11*, 45. [CrossRef]
8. Feloni, E. Assessment of Flood Induced by Heavy Rainfall Using Advanced Methodologies, as a Premise for an Integrated Flood Early Warning System: The Case of Attica Region. Ph.D. Thesis, National Technical University of Athens, Zografou, Greece, 2019.
9. Berne, A.; Delrieu, G.; Creutin, J.-D.; Obled, C. Temporal and Spatial Resolution of Rainfall Measurements Required for Urban Hydrology. *J. Hydrol.* **2004**, *299*, 166–179. [CrossRef]
10. Merz, R.; Blöschl, G. A Process Typology of Regional Floods. *Water Resour. Res.* **2003**, *39*, 1340. [CrossRef]
11. Houze, R.A., Jr.; Rasmussen, K.L.; Zuluaga, M.D.; Brodzik, S.R. The Variable Nature of Convection in the Tropics and Subtropics: A Legacy of 16 Years of the Tropical Rainfall Measuring Mission Satellite. *Rev. Geophys.* **2015**, *53*, 994–1021. [CrossRef]
12. Velásquez, N.; Hoyos, C.D.; Vélez, J.I.; Zapata, E. Reconstructing the 2015 Salgar Flash Flood Using Radar Retrievals and a Conceptual Modeling Framework in an Ungauged Basin. *Hydrol. Earth Syst. Sci.* **2020**, *24*, 1367–1392. [CrossRef]
13. Bournas, A.; Baltas, E. Investigation of the Gridded Flash Flood Guidance in a Peri-Urban Basin in Greater Athens Area, Greece. *J. Hydrol.* **2022**, *610*, 127820. [CrossRef]
14. Binetti, M.S.; Campanale, C.; Massarelli, C.; Uricchio, V.F. The Use of Weather Radar Data: Possibilities, Challenges and Advanced Applications. *Earth* **2022**, *3*, 157–171. [CrossRef]
15. Rapant, P.; Kolejka, J. Dynamic Pluvial Flash Flooding Hazard Forecast Using Weather Radar Data. *Remote Sens.* **2021**, *13*, 2943. [CrossRef]
16. Costabile, P.; Costanzo, C.; Kalogiros, J.; Bellos, V. Toward Street-Level Nowcasting of Flash Floods Impacts Based on HPC Hydrodynamic Modeling at the Watershed Scale and High-Resolution Weather Radar Data. *Water Resour. Res.* **2023**, *59*, e2023WR034599. [CrossRef]
17. Novák, P.; Kyznarová, H.; Pecha, M.; Šercl, P.; Svoboda, V.; Ledvinka, O. Utilization of Weather Radar Data for the Flash Flood Indicator Application in the Czech Republic. *Remote Sens.* **2021**, *13*, 3184. [CrossRef]
18. Cho, J.Y.N.; Kurdzo, J.M. Weather Radar Network Benefit Model for Flash Flood Casualty Reduction. *J. Appl. Meteorol. Climatol.* **2020**, *59*, 589–604. [CrossRef]
19. Nikolopoulos, E.I.; Anagnostou, E.N.; Borga, M. Using High-Resolution Satellite Rainfall Products to Simulate a Major Flash Flood Event in Northern Italy. *J. Hydrometeorol.* **2013**, *14*, 171–185. [CrossRef]
20. Thielen, J.; Bartholmes, J.; Ramos, M.-H.; Roo, A. de The European Flood Alert System–Part 1: Concept and Development. *Hydrol. Earth Syst. Sci.* **2009**, *13*, 125–140. [CrossRef]
21. Alfieri, L.; Thielen, J. A European Precipitation Index for Extreme Rain-Storm and Flash Flood Early Warning. *Meteorol. Appl.* **2015**, *22*, 3–13. [CrossRef]
22. Raynaud, D.; Thielen, J.; Salamon, P.; Burek, P.; Anquetin, S.; Alfieri, L. A Dynamic Runoff Co-Efficient to Improve Flash Flood Early Warning in Europe: Evaluation on the 2013 Central European Floods in Germany: Dynamic Runoff Co-Efficient for Flash Flood Early Warning in Europe. *Meteorol. Appl.* **2015**, *22*, 410–418. [CrossRef]
23. Park, S.; Berenguer, M.; Sempere-Torres, D.; Baugh, C.; Smith, P. *Toward Seamless High-Resolution Flash Flood Forecasting over Europe Based on Radar Nowcasting and NWP: An Evaluation with Case Studies*; ADS: Washington, DC, USA, 2017; p. 12158.
24. Park, S.; Berenguer, M.; Sempere-Torres, D. Long-Term Analysis of Gauge-Adjusted Radar Rainfall Accumulations at European Scale. *J. Hydrol.* **2019**, *573*, 768–777. [CrossRef]
25. Anagnostou, M.; Nikolopoulos, E.; Kalogiros, J.; Anagnostou, E.; Marra, F.; Mair, E.; Bertoldi, G.; Tappeiner, U.; Borga, M. Advancing Precipitation Estimation and Streamflow Simulations in Complex Terrain with X-Band Dual-Polarization Radar Observations. *Remote Sens.* **2018**, *10*, 1258. [CrossRef]
26. Bournas, A.; Baltas, E. Comparative Analysis of Rain Gauge and Radar Precipitation Estimates towards Rainfall-Runoff Modelling in a Peri-Urban Basin in Attica, Greece. *Hydrology* **2021**, *8*, 29. [CrossRef]
27. Georgakakos, K.P.; Modrick, T.M.; Shamir, E.; Campbell, R.; Cheng, Z.; Jubach, R.; Sperfslage, J.A.; Spencer, C.R.; Banks, R. The Flash Flood Guidance System Implementation Worldwide: A Successful Multidecadal Research-to-Operations Effort. *Bull. Am. Meteorol. Soc.* **2022**, *103*, E665–E679. [CrossRef]
28. Georgakakos, K.P. Analytical Results for Operational Flash Flood Guidance. *J. Hydrol.* **2006**, *317*, 81–103. [CrossRef]
29. Sweeney, T.L. *Modernized Areal Flash Flood Guidance*; NOAA Technical Memorandum NWS Hydro 44: Silver Spring, MD, USA, 1992.
30. Smith, G.; Flash Flood Potential: Determining the Hydrologic Response of FFMP Basins to Heavy Rain by Analyzing Their Physiographic Characteristics. A White Paper Available from the NWS Colorado Basin River Forecast Center. 2003. Available online: http://www.cbrfc.noaa.gov/papers/ffp_wpap.pdf (accessed on 1 November 2024).
31. Schmidt, J.A.; Anderson, A.J.; Paul, J.H. Spatially-Variable, Physically-Derived Flash Flood Guidance. In Proceedings of the Preprints, 21st Conference on Hydrology, San Antonio, TX, USA, 14–18 January 2007; Meteorology and Climatology B. Volume 6.

32. Clark, R.A.; Gourley, J.J.; Flamig, Z.L.; Hong, Y.; Clark, E. CONUS-Wide Evaluation of National Weather Service Flash Flood Guidance Products. *Weather Forecast.* **2014**, *29*, 377–392. [CrossRef]
33. Hapuarachchi, H.A.P.; Wang, Q.J.; Pagano, T.C. A Review of Advances in Flash Flood Forecasting. *Hydrol. Process.* **2011**, *25*, 2771–2784. [CrossRef]
34. Zeng, Z.; Tang, G.; Long, D.; Zeng, C.; Ma, M.; Hong, Y.; Xu, H.; Xu, J. A Cascading Flash Flood Guidance System: Development and Application in Yunnan Province, China. *Nat. Hazards* **2016**, *84*, 2071–2093. [CrossRef]
35. Baltas, E.A. A New Approach for the Determination of Hydrologic Prefectures in Greece for the Water Framework Directive. *New Medit* **2008**, *7*, 41–47.
36. Bournas, A.; Baltas, E. Development of a Storm-Tracking Algorithm for the Analysis of Radar Rainfall Patterns in Athens, Greece. *Water* **2024**, *16*, 2905. [CrossRef]
37. Bournas, A.; Baltas, E. Determination of the Z-R Relationship through Spatial Analysis of X-Band Weather Radar and Rain Gauge Data. *Hydrology* **2022**, *9*, 137. [CrossRef]
38. Bournas, A.; Baltas, E. Analysis of Weather Radar Datasets through the Implementation of a Gridded Rainfall-Runoff Model. *Environ. Process.* **2022**, *10*, 7. [CrossRef]
39. Lagouvardos, K.; Kotroni, V.; Koussis, A.; Feidas, H.; Buzzi, A.; Malguzzi, P. The Meteorological Model BOLAM at the National Observatory of Athens: Assessment of Two-Year Operational Use. *J. Appl. Meteorol. Climatol.* **2003**, *42*, 1667–1678. [CrossRef]
40. Mariani, S.; Casaioli, M.; Coraci, E.; Malguzzi, P. A New High-Resolution BOLAM-MOLOCH Suite for the SIMM Forecasting System: Assessment over Two HyMeX Intense Observation Periods. *Nat. Hazards Earth Syst. Sci.* **2015**, *15*, 1–24. [CrossRef]
41. Papadopoulos, A.; Katsafados, P.; Kallos, G.; Nickovic, S. The Weather Forecasting System for Poseidon—An Overview. *J. Atmos. Ocean Sci.* **2002**, *8*, 219–237. [CrossRef]
42. Varlas, G.; Papadopoulos, A.; Papaioannou, G.; Dimitriou, E. Evaluating the Forecast Skill of a Hydrometeorological Modelling System in Greece. *Atmosphere* **2021**, *12*, 902. [CrossRef]
43. Varlas, G.; Spyrou, C.; Papadopoulos, A.; Korres, G.; Katsafados, P. One-Year Assessment of the CHAOS Two-Way Coupled Atmosphere-Ocean Wave Modelling System over the Mediterranean and Black Seas. *Mediterr. Mar. Sci.* **2020**, *21*, 372–385. [CrossRef]
44. Carpenter, T.M.; Sperfslage, J.A.; Georgakakos, K.P.; Sweeney, T.; Fread, D.L. National Threshold Runoff Estimation Utilizing GIS in Support of Operational Flash Flood Warning Systems. *J. Hydrol.* **1999**, *224*, 21–44. [CrossRef]
45. Reed, S.; Johnson, D.; Sweeney, T. Application and National Geographic Information System Database to Support Two-Year Flood and Threshold Runoff Estimates. *J. Hydrol. Eng.* **2002**, *7*, 209–219. [CrossRef]
46. Erlingis, J.M.; Gourley, J.J.; Hong, Y. Relationships between Return Period and Flash Flooding in the United States. *AGU Fall Meet. Abstr.* **2013**, *2013*, H51Q-04.
47. Koutsoyiannis, D. *Stochastics of Hydroclimatic Extremes—A Cool Look at Risk*; Kallipos, Open Academic Editions: Athens, Greece, 2021; ISBN 978-618-85370-0-2.
48. Iliopoulou, T.; Malamos, N.; Koutsoyiannis, D. Regional Ombrian Curves: Design Rainfall Estimation for a Spatially Diverse Rainfall Regime. *Hydrology* **2022**, *9*, 67. [CrossRef]
49. Koutsoyiannis, D.; Iliopoulou, T.; Koukouvinos, A.; Malamos, N. A Stochastic Framework for Rainfall Intensity–Time Scale–Return Period Relationships. Part I: Theory and Estimation Strategies. *Hydrol. Sci. J.* **2024**, *69*, 1082–1091. [CrossRef]
50. USDA Natural Resources Conservation Service (NRCS). *National Engineering Handbook: Part 630—Hydrology*; USDA Soil Conservation Service: Washington, DC, USA, 2004.
51. Baltas, E.A.; Dervos, N.A.; Mimikou, M.A. Determination of the SCS Initial Abstraction Ratio in an Experimental Watershed in Greece. *Hydrol. Earth Syst. Sci.* **2007**, *11*, 1825–1829. [CrossRef]
52. Marshall, J.S.; Palmer, W.M.K. The Distribution of Raindrops with Size. *J. Meteorol.* **1948**, *5*, 165–166. [CrossRef]
53. Zeng, Z.; Wang, D.; Chen, Y. An Investigation of Convective Features and Z-R Relationships for a Local Extreme Precipitation Event. *Atmos. Res.* **2021**, *250*, 105372. [CrossRef]

Disclaimer/Publisher's Note: The statements, opinions and data contained in all publications are solely those of the individual author(s) and contributor(s) and not of MDPI and/or the editor(s). MDPI and/or the editor(s) disclaim responsibility for any injury to people or property resulting from any ideas, methods, instructions or products referred to in the content.